Back contact interfacial modification mechanism in highly-efficient antimony selenide thin-film solar cells

Junhui Lin, Guojie Chen, Nafees Ahmad, Muhammad Ishaq, Shuo Chen, Zhenghua Su, Ping Fan, Xianghua Zhang, Yi Zhang, Guangxing Liang

To cite this version:

Junhui Lin, Guojie Chen, Nafees Ahmad, Muhammad Ishaq, Shuo Chen, et al.. Back contact interfacial modification mechanism in highly-efficient antimony selenide thin-film solar cells. Journal of Energy Chemistry, 2023, 80, pp.256-264. 10.1016/j.jechem.2023.01.049 . hal-04057768

HAL Id: hal-04057768

https://hal.science/hal-04057768v1

Submitted on 12 May 2023

Back contact interfacial modification mechanism in highly-efficient antimony selenide thin-film solar cells

*Jun-Hui Lin[1], Guo-Jie Chen[1], Nafees Ahmad[1], Muhammad Ishaq[2], Shuo Chen[1], Zheng-Hua Su[1], Ping Fan[1], Xiang-Hua Zhang[3], Yi Zhang[4], Guang-Xing Liang[1]**

[1.] Shenzhen Key Laboratory of Advanced Thin Films and Applications, Key Laboratory of Optoelectronic Devices and Systems of Ministry of Education and Guangdong Province, College of Physics and Optoelectronic Engineering, Shenzhen University, Shenzhen 518060, Guangdong, China.

[2.] Institute of Fundamental and Frontier Science, University of Electronic Science and Technology of China. Chengdu 610054, Sichuan, China

[3.] Univ Rennes, CNRS, ISCR (Institut des Sciences Chimiques de Rennes) UMR 6226, Rennes, F-35000, France

[4.] Institute of Photoelectronic Thin Film Devices and Technology and Tianjin Key Laboratory of Thin Film Devices and Technology, Nankai University, Tianjin 300350, China.

*Corresponding author. E-mail address: lgx@szu.edu.cn (Prof. Liang).

Keywords: Sb_2Se_3 solar cells; MoO_2 intermediate layer; Back contact; Defects

Abstract: Antimony selenide (Sb_2Se_3) is a potential photovoltaic (PV) material for next-generation solar cells and has achieved great development in the last several years. The properties of Sb_2Se_3 absorber and back contact influence the PV performances of Sb_2Se_3 solar cells. Hence, optimization of back contact characteristics and absorber orientation are crucial steps in raising the power conversion efficiency (PCE) of Sb_2Se_3 solar cells. In this work, MoO_2 was introduced as an intermediate layer (IL) in Sb_2Se_3 solar cells, and comparative investigations were conducted. The growth of (211)-oriented Sb_2Se_3 with large grains was facilitated by introducing the MoO_2 IL with suitable thickness. The MoO_2 IL substantially lowered the back contact barrier and prevented the formation of voids at the back contact, which reduced the thickness of the $MoSe_2$ interface layer, inhibited carrier recombination, and minimized bulk and interfacial defects in devices. Subsequently, significant optimization enhanced the open-circuit voltage (V_{OC}) of solar cells from 0.481 V to 0.487 V, short-circuit current density (J_{SC}) from 23.81 mA/cm^2 to 29.29 mA/cm^2, and fill factor from 50.28% to 57.10%, which boosted the PCE from 5.75% to 8.14%.

1. Introduction

Solar energy holds the promise of carbon-free energy that can be used to meet our energy demands. Si-based solar cells have the highest power conversion efficiency (PCE); it contributes significantly to photovoltaic (PV) devices with a PCE of more than 26.8% [1]. However, the low absorption coefficient and high processing cost of Si are major issues that limit its future application for the development of highly efficient and low-cost PVs. Compound-based solar cells, such as perovskites, copper-indium-gallium-selenide ($Cu(In,Ga)Se_2$), and cadmium telluride (CdTe), have attracted huge attention and have attained PCE values higher than 21% [1]. However, the instability of perovskites, the toxic nature of Cd, and the low natural abundances of In and Ga are important issues in scaling up this technology. Therefore, research is being conducted on stable and environment-friendly PV semiconductor materials. Among various photoactive materials, antimony selenide (Sb_2Se_3) thin films have an appropriate band gap, suitable absorption coefficient, and good conductivity [2–5]. Furthermore, their high theoretically attainable PCE (more than 30%) makes them potential candidates for the future generation of PVs [6]. Sb_2Se_3 solar cells have drawn huge interest, and their performances have gradually improved. The reported PCE of Sb_2Se_3 solar cells have increased promptly from 1.9% to 10.57% [2,3,7–15]. The series-connected antimony selenosulfide monolithic integrated PV minimodules have achieved PCE of 7.15% [16]. Tang's group prepared Sb_2Se_3 photo-absorber film by thermal evaporation method and obtained 2.1% efficiency [17]. Afterward, the rapid thermal evaporation method was used to tune the crystal orientation of Sb_2Se_3, which raised the PCE up to 5.6% [18]. In 2018, the same research group prepared a high-quality Sb_2Se_3 absorber layer by vapor transporting deposition, and the defect concentration of the Sb_2Se_3 absorber layer was reduced [3]. The Sb_2Se_3 device exhibited a PCE of 7.6%. Mai et al. fabricated Sb_2Se_3 nanorod array by close space sublimation process and gained a much-improved PCE of 9.2% [2]. Chen's group fabricated $Sb_2(S, Se)_3$ solar cells with a PCE of 10% by hydrothermal method [19]. However, the PCE values were still considerably lower than the theoretical limits (PCE = 30%) of the Sb_2Se_3 device. Sb_2Se_3 PVs have shown exceptional performances with the device configuration of Mo/Sb_2Se_3/CdS/indium tin oxide (ITO)/Ag, similar to CZTS and CdTe solar cells [20,21]. Back contact engineering is one of the best strategies for improving the PV parameters (V_{OC}, J_{SC}, and fill factor (FF)) of chalcogenide thin-film solar cells [22]. The characteristics of Mo/Sb_2Se_3 back contact play a significant role in photo-generated carrier transport in Sb_2Se_3 devices, where the low barrier of Mo/Sb_2Se_3 back contact is important to achieve a high PCE. In addition, a $MoSe_2$ layer was observed between Sb_2Se_3 and Mo electrode [23]. A thick $MoSe_2$ interface layer may be harmful to the transport of carriers at the Mo/Sb_2Se_3 back contact, which reduces the PCE of Sb_2Se_3 solar cells. In our previous work, (211)-oriented Mo not only induced the growth of (hk1)-oriented Sb_2Se_3 but also improved the ohmic contact at the Mo/Sb_2Se_3 back interface due to the existence of $MoSe_2$ layer [24]. The ohmic contact of Mo/Sb_2Se_3 interface can be improved by further reducing the thickness of $MoSe_2$ interface appropriately. Thus, further optimization of the back contact of Sb_2Se_3 may lead to the auxiliary promotion of PCE. Relatively, less attention has been given to the modification of back contact (Mo/Sb_2Se_3) of the device structure of Mo/Sb_2Se_3/CdS/ITO/Ag. Mo selenization was used to prepare the $MoSe_2$ intermediate layer (IL) at the back contact to boost the PCE of Sb_2Se_3 solar cells, but the PCE of Sb_2Se_3 solar cells was limited to 5% [25]. Thus, a better back contact modification of Sb_2Se_3 solar cells is needed for detailed investigation. In this study, we adopted an ambient pre-annealing process to prepare the MoO_2 layer between Sb_2Se_3 absorber layer and Mo substrate in Sb_2Se_3 solar cells. The MoO_2 layer suppressed the formation of $MoSe_2$ interface layer, and the Mo/Sb_2Se_3 back contact barrier was abridged. Compared with Sb_2Se_3 solar cells (without MoO_2 IL), the V_{OC} of Sb_2Se_3 solar cells increased from 0.481 V to 0.487 V, the J_{SC} increased from 23.81 mA/cm^2 to 29.29 mA/cm^2, and FFFF increased from 50.28% to 57.10%, which led to a final PCE of 8.14% with the MoO_2 IL. Afterward, the effect of MoO_2 IL on the Sb_2Se_3 properties, interface properties, carrier diffusion length, and defect properties of devices were explored. In addition, the influence of annealing temperature on the thickness of MoO_2 layer was thoroughly investigated.

2. Experimental

2.1. Preparation of MoO_2 intermediate layer

First, substrates (Mo-coated glass) were washed with ethanol, detergent, and distilled water by ultrasonication. The cleaned Mo substrates were annealed in the furnace under the air flow to grow the MoO_2 IL. Here, the annealing temperatures of samples were kept at 300 ℃ and 400 ℃. The annealing duration of samples was 15 min. The unannealed sample was labeled as Mo1, and the samples annealed at 300 ℃ and 400 ℃ were respectively labeled as Mo2 and Mo3.

2.2. Preparation of Sb_2Se_3 thin films

The Sb precursors were prepared on Mo1, Mo2, and Mo3 substrates by radio frequency magnetron sputtering at very low pressure (below 5.0×10^{-4} Pa). The flow rate of Ar was 40 sccm, the sputtering power of Sb was kept at 34 W, the sputtering time of Sb metal precursor was 40 min, and the sputtering pressure for deposition of Sb was 1 Pa. Subsequently, Sb_2Se_3 was fabricated by post-selenization of the Sb layer. The Se (0.4 g) and Sb metal precursors were kept in the compartment. The evacuation process was conducted, and argon was introduced into the furnace prior to selenization. The selenization pressure for all samples was 7×10^4 Pa. The selenization temperature of Sb_2Se_3 on Mo1, Mo2, and Mo3 substrates was 410 ℃. The ramping rate for all selenized samples was 20 ℃/min, and the selenization time of all samples was 15 min. Three samples were labeled as S_{Mo1}, S_{Mo2}, and S_{Mo3}.

2.3. Fabrication of Sb_2Se_3 solar cells

Cadmium sulfide (CdS) as a buffer layer was deposited onto the S_{Mo1}, S_{Mo2}, and S_{Mo3} samples by a chemical bath deposition method. The mixed solution was prepared by mixing cadmium sulfate (0.015 M), NH_3OH aqueous solution, water, and thiourea (0.75 M). The Sb_2Se_3 absorber was vertically dipped in the solution at 85 ℃ with continuous stirring for at least 9 min. The

CdS films were put into the oven for 30 min to remove excess solution from the surface. The Sb_2Se_3/CdS heterojunction was heated at 325 ℃ in a vacuum, and the annealing time of all samples was 5 min. Afterward, the ITO layers were sputtered on the top surface of CdS buffer layers. Sputtering pressure (0.4 Pa), sputtering time (25 min), and sputtering power (120 W) were kept the same for all devices. Finally, the Ag electrodes were deposited by thermal evaporation. The device area measured 0.09 cm^2 after scabbing. The three devices were labeled as S_{Mo1}, $S_{Mo2,}$ and S_{Mo3}.

2.4. Characterizations

The crystal phases of MoO_2 ILs and Sb_2Se_3 thin films were analyzed by X-ray diffraction (XRD, Ultima-iv) with Cu K_α radiation. To further investigate the crystal phases of MoO_2 thin films, we analyzed the samples by Raman spectroscopy (HORIBA Jobin Yvon, LabRAM HR Evolution) with an excitation wavelength of 532 nm. Film morphologies of samples were obtained by the scanning electron microscopy (SEM, Zeiss SUPRA 55). Energy dispersive X-ray spectroscopy (EDS, BRUKER QUANTAX 200) was utilized for the characterization of sample elemental compositions. The transmission electron microscopy (TEM) images of sample cross-sectional morphologies were obtained by FEI Titan Cubed ThemisG2 300 microscope. The samples for TEM imaging were fabricated by a focused ion beam (FEI Scios). The elemental depth distribution of devices was obtained by TEM coupled with EDS. The ohmic contact properties of Mo/Sb_2Se_3 back contact were tested by a multi-meter (Keithley, 2400 Series). The work functions of samples were analyzed by ultraviolet-photoelectron spectroscopy (UPS, Thermo Scientific ESCALAB 250Xi). The current density-voltage (*J-V*) of solar cells was measured by a multi-meter (Keithley, 2400 Series) under standard test conditions (100 mW/cm^2, AM 1.5 G). The dark *J-V* curves of solar cells were also measured by a multi-meter (Keithley, 2400 Series). A Keithley 2400 source meter and Zolix SCS101 system were used to test the external quantum efficiency (EQE) of solar cells. Temperature-dependent dark *J-V* measurements were characterized by Lakeshore 325 temperature controller, and the temperatures were swept from 300 K to 230 K in a step of 10 K. The capacitance-voltage (*C-V*) measurements and drive level capacitance (DLCP) measurements were characterized by a Keithley 4200A-SCS system with JANIS cryogenic platform. The measurement of temperature-dependent V_{OC} was utilized by the Lakeshore 325 temperature controller. The electrochemical impedance spectroscopy (EIS) of devices was characterized by the CHI600E electrochemical workstation. Temperature-dependent capacitance frequency (*C-f-T*) measurements were carried out within the frequency range of 100 Hz to 10 MHz using the same cryostat and cooling system as mentioned above.

3. Result and discussion

XRD analysis was performed to study the effect of air on the annealing of Mo. The XRD results (Fig. S1a) showed the presence of MoO_2 crystal phases (JCPDS#32-0671) at Mo back electrodes. Furthermore, the Raman spectra (Fig. S1b) indicated the formation of MoO_2 phases on the surfaces of Mo substrates. The presence and thickness of MoO_2 ILs are depicted in Fig, S2, where Mo1 represents the sample without air annealing, Mo2 denotes the sample annealed at 300 °C, and the sample annealed at 400 °C was labeled as Mo3. Samples Mo2 and Mo3 exhibited compact and smooth layers of MoO_2 having a thickness of 80 and 800 nm, respectively. Fig. 1(a) shows the cross-sectional morphology of the full device (Mo/Sb_2Se_3/CdS/ITO/Ag) fabricated on the sample Mo2, which is labeled as $S_{Mo2.}$ MoO_2 layer with a thickness of 80 nm can be observed at Sb_2Se_3/Mo back electrode. This finding demonstrates that the selenization process has no effect on the thickness of MoO_2 layer. In contrast to the SEM image (Fig. S3) of the S_{Mo1} device, the $MoSe_2$ interface layer was not visible at the Mo/Sb_2Se_3 back contact in the S_{Mo2} device. Thus, the MoO_2 layer suppressed the formation of $MoSe_2$ layer. The (211)-oriented Sb_2Se_3 has large grains penetrating through the full absorber layer in the S_{Mo2} device. On the other hand, a comparatively more dominant (221) oriented Sb_2Se_3 absorber layer can be observed in the SEM image of S_{Mo1} devices (Fig. S3), consistent with the XRD results. According to the literature, the PCE of the Sb_2Se_3 device with (211)-oriented Sb_2Se_3 is more dominant than the (221)-oriented Sb_2Se_3 [26]. In addition to the favored orientation, the back contact of the S_{Mo2} device featured a compact and void-free interface (Fig. 1a) in comparison with that of the S_{Mo1} device (Fig. S3). These findings demonstrate that the morphology of the Mo/Sb_2Se_3 back contact was enhanced by the MoO_2 IL. Fig. 1(b) illustrates the *J-V* characteristic of S_{Mo1}, S_{Mo2}, and S_{Mo3} devices. The S_{Mo1} device had a V_{OC} of 0.481 V, a J_{SC} of 23.81 mA/cm^2, a FF of 50.28%, and a PCE of 5.75%. When the MoO_2 IL with a thickness of 80 nm was introduced at the back contact of S_{Mo2} device, all the PV parameters of S_{Mo2} device increased. The S_{Mo2} device delivered a V_{OC} of 0.487 V, J_{SC} of 29.29 mA/cm^2, and FF of 57.10%, thus achieving a PCE of 8.14%. The $V_{OC\text{-deficit}}$ decreased from 829 mV in S_{Mo1} device to 793 mV in S_{Mo2} device indicating the better performance due to the MoO_2 introduction. In addition, the MoO_2 layer with a thickness of 800 nm resulted in PV performance degradation. The S_{Mo3} device obtained a low PCE of 4.18% with a V_{OC}, J_{SC}, and FF of 0.424 V, 21.52 mA/cm^2, and 45.76%, respectively. The resistances of MoO_2 IL increased as the thickness further increased. The Mo/Sb_2Se_3 back contact with the high resistance limited the transport of photo-generated carrier, which led to performance degradation. All photovoltaic parameters were shown in Table 1. Fig. S4 summarizes the statistical distribution performances of the device parameters. Fig. 1(c) presents the *J-V* parameters of S_{Mo1} and S_{Mo2} devices under light and dark conditions. The existence of a back contact barrier led to the crossover behavior among the light and dark *J-V* curves besides the double diode performance [27]. Compared with S_{Mo2} device with MoO_2 IL, the crossover points occurred at a lower current in the S_{Mo1} device. According to the literature, the crossover behavior at a low current is attributed to the high back contact barrier in solar cells [28]. Thus, the high back contact barrier height may be present in S_{Mo1} devices. In addition, the collection of photogenerated holes mainly depends on the Mo/$MoSe_2$ interface. Thus, we further investigated the barrier of Mo/$MoSe_2$ in the S_{Mo1} device. Fig. S5 shows the UPS spectra of $MoSe_2$, Sb_2Se_3, MoO_2, and Mo. The barrier heights of Mo/$MoSe_2$, Mo/MoO_2, and MoO_2/Sb_2Se_3 were 0.55, 0.02, and 0.03 eV, respectively. Fig. 1(d and e) presents the band diagrams of S_{Mo1} and S_{Mo2} devices. Fig. S6 reveals the effects of the MoO_2 layer on the EQE of solar cells, band gap, and Urbach energy of the absorber. Figs. S6(a and b) show the EQE of S_{Mo1} and S_{Mo2} devices, respectively. The EQE results demonstrate that the S_{Mo2} device had a higher J_{SC} than the S_{Mo1} device due to its superior carrier collection efficiency. Better crystal orientation improved crystalline quality, and a reduced $MoSe_2$ interface layer all contributed to the improved J_{SC}, which also resulted in a higher FF [28]. The band gaps of Sb_2Se_3 in S_{Mo1} and S_{Mo2} devices measured 1.31 and 1.28 eV, respectively (Fig. S6c). Thus, the MoO_2 IL can change the band gap of the Sb_2Se_3 absorber layer. Fig. S6(d) shows the Urbach energy (E_u) of Sb_2Se_3 attained from EQE. The E_u parameter is used to evaluate the band tail states because of impurities, defects, and disorders in photo-absorber materials [24]. An E_u of 22.3 meV indicated the reduction of defect states due to the introduction of MoO_2 IL. The roles of MoO_2 IL include obtaining the ideal orientation of Sb_2Se_3, limiting the growth of $MoSe_2$ interface layer, lowering the back contact barrier, promoting grain growth, and increasing minority carrier diffusion length. These functions of MoO_2 IL in the device need to be investigated in detail.

Fig. 2(a) shows the XRD data of the Sb_2Se_3 film on Mo1, Mo2, and Mo3 substrates. All the peaks of S_{Mo1}, S_{Mo2}, and S_{Mo3} samples were in good match with JCPDS (No. 15-0861) with no secondary phases. Each sample exhibited the preferred (211), (221), and (002) orientations of Sb_2Se_3 with minimal fluctuation, which is expected to demonstrate variation in the solar cell performance. Compared with S_{Mo1}, the I(211)/I(221) intensity ratio of S_{Mo2} sample increased from 1.01 to 1.28, inducing the formation of (211)-oriented Sb_2Se_3 layer upon the insertion of 80 nm MoO_2 IL. However, an extremely thick MoO_2 layer reduced the I(211)/I(221) intensity ratio from 1.28 to 0.87. Thus, an overly thick MoO_2 layer limits the growth of (hk1)-oriented Sb_2Se_3. These findings were further authenticated by evaluating the texture coefficient (TC) of Sb_2Se_3 peaks (Fig. 2b), which can be calculated by Equation (1) [29]

$$TC_{hkl} = \frac{I_{(hkl)}}{I_{0(hkl)}} \Bigg/ \left(\frac{1}{N} \sum_{i=1}^{N} \frac{I_{(h_i k_i l_i)}}{I_{0(h_i k_i l_i)}} \right) \qquad (1)$$

where the peak intensities of planes hkl are $I_{0(hkl)}$ and $I_{(hkl)}$ in the standard and measured XRD patterns of Sb_2Se_3 thin films, respectively. A large TC value indicates the preferred orientation along a specific direction [30]. Compared with S_{Mo1} and S_{Mo3} samples, the TC value of S_{Mo2} sample's (211) peak was higher. When the thickness (MoO_2) increased from 0 nm to 80 nm, the TC value of S_{Mo2} sample's (211) peak increased and then declined with the further increase in thickness. Fig. 2(c-e) displays the images of surface morphologies of S_{Mo1}, S_{Mo2}, and S_{Mo3} samples. Alongside the preferred orientation, the S_{Mo2} sample also showed compact, flat, and large-grained surface morphology, whereas the other two samples comprised comparatively smaller grains and several voids (Fig. 2c-e). Fig. 2(f) shows the plotted porosity and average crystal size of Sb_2Se_3, which indicates that the S_{Mo2} sample had larger crystal sizes and fewer pin holes. These results demonstrated that the MoO_2 IL with 80 nm-thickness was obliged to the growth of (211)-oriented Sb_2Se_3 with large grains. The champion S_{Mo2} sample was Sb-poor and Se-rich as listed in Table S1.

To further study the interface morphologies of Mo/Sb_2Se_3 in S_{Mo2} solar cells, we captured the TEM images of S_{Mo2} devices (Fig. 3). ITO, window layer, a buffer layer (CdS), Sb_2Se_3 absorber layer, MoO_2 IL, and Mo back electrode of S_{Mo2} device were observed from the top to the bottom in Fig. 3(a). High-angle annular dark field scanning–transmission electron microscopy) was performed at the heterojunction interface of Sb_2Se_3/CdS in Fig. 3(b). The interface of Sb_2Se_3/CdS was indistinct, which implies less lattice mismatch between Sb_2Se_3 and CdS. Fig. 3(c) shows the TEM image of back contact ($Mo/MoO_2/Sb_2Se_3$). A distinct interface with flattened and tacky contact can be observed at the Mo/MoO_2 and MoO_2/Sb_2Se_3 interfaces. The absence of dislocation, amorphous layer, or crystal lattice distortion at the Mo/MoO_2 and MoO_2/Sb_2Se_3 interfaces is expected to be applied to establish efficient charge carrier generation and transport. Fig. 3(d-f) displays the high-resolution TEM images of Sb_2Se_3 absorber layer,

MoO_2 IL, and Mo electrode in the device. To further examine the preferred orientation of each layer, we examined the electron diffraction patterns of Sb_2Se_3, MoO_2, and Mo using Fourier transform (Fig. 3g–i). In Fig. 3(g), the (221), (211), and (002) planes of Sb_2Se_3 can be observed. Fig. 3(h) illustrates the (011), (-211), and (022) planes of MoO_2, whereas Fig. 3(i) illustrates the (110) and (211) planes of Mo. These results for electron diffraction patterns were consistent with the XRD findings. The TEM-coupled EDS elemental line scans were used to explore the effect of IL (MoO_2) on the element distribution of device back contact (Fig. S7). The thickness of MoO_2 was about 90 nm. The distribution of Mo at the Mo/Sb_2Se_3 interface implied that Mo is very stable during selenization. The Sb, Se, and O atoms diffused into the Mo electrode. The diffusion of Sb, Se, and O atoms may have no influence on the PV properties of Sb_2Se_3.

To elucidate the role of MoO_2 IL on the back contact barrier of Sb_2Se_3 device, we studied the ohmic contact of Mo/Sb_2Se_3 and series resistance (R_s). Fig. S8(a) shows the I-V curves obtained from the device structure of glass/Mo/Sb_2Se_3/Ag. All linear curves (I-V) suggest ohmic contact formation at the Mo/Sb_2Se_3 interface. Fig. S8(b) illustrates the resistance curves and slopes of all samples. The slopes of S_{Mo1}, S_{Mo2}, and S_{Mo3} measured 0.071, 0.101, and 0.039 S, respectively. Their corresponding resistances were 14.08, 9.90, and 25.64 Ω. The S_{Mo2} device exhibited the largest slope indicating the lowest resistivity and it can improve the ohmic behavior at the Mo/MoO_2/Sb_2Se_3 back contact which is favorable for the efficient transport of photogenerated holes [24]. J-V-T curves of devices were also characterized at the temperature range of 230–300 K in a dark environment (Fig. 4a and b). R_s and barrier heights of the back contact diode were obtained from the result of dark J-V-T [31,32]. Fig. 4(c) shows the temperature-dependent R_s. The R_s of the S_{Mo1} device increased 20 times from 300 K to 230 K, compared with the 4 times increased observed for the S_{Mo2} device. The contact barrier (Φ_B) at the Mo/Sb_2Se_3 led to a high R_s value at low temperatures. The transport of photogenerated carriers was suppressed by hindering the contact barrier. At low temperatures, the back contact diode term is dominated by fitting the corresponding linear region of ln (R_sT) versus 1/T plot in Fig. 4(d). The Φ_B of S_{Mo1}

and S_{Mo2} devices were 217 and 73.9 meV, respectively. The smaller barrier existed at the back contact of S_{Mo2} device. In addition, the *J-V-T* analysis was a useful method used to determine a dominant recombination path present in Sb_2Se_3 solar cells by plotting $A\ln(J_0)$ against $1/kT$ (Fig. 4e). The $A\ln(J_0)$ versus $1/kT$ data should yield a straight line and extrapolate to the activation energy E_A/q at T=0 K. The activation energy (E_A) of recombination for the S_{Mo1} device was 0.71 eV, and that for S_{Mo2} device was 1.18 eV. The bandgap of Sb_2Se_3 thin films can be obtained from EQE, and the calculated bandgaps of S_{Mo1} and S_{Mo2} were 1.31 and 1.28 eV, respectively (Fig. S6). The E_A for the S_{Mo1} device was considerably lower than the band gap of Sb_2Se_3 in S_{Mo1} device, which suggests that the recombination mechanism of S_{Mo1} device was mainly influenced by interface recombination. The E_A for the S_{Mo2} device was relatively close to the band gap of Sb_2Se_3 in S_{Mo2} device, which signified the passivation of recombination at the interface. Fig. 4(f) presents a model of the back contact junction of Sb_2Se_3 solar cell as a Schottky diode. The circuit model includes two diodes: the main solar cell diode (D_{SC}) and back contact diode (D_{BC}) [31]. When the solar cell is forward-biased, the back contact diode is in reverse bias. The reversed biased D_{BC} is detrimental to the output of photo-generated current. Therefore, MoO_2 IL reduces the back contact barrier value, which significantly mitigates the depraved effect of reversed biased D_{BC} on the output of photo-generated current.

The interfacial defects and bulk defects of S_{Mo1} and S_{Mo2} devices were also investigated by *C-V* and DLCP measurements (Fig. 5a). The DLCP (N_{DLCP}) is solely sensitive to responses from bulk defects and free carriers, whereas the *C-V* ($N_{C\text{-}V}$) theoretically incorporates responses from interfacial defects, bulk defects, and free carriers [6,10]. Thus, the interfacial defects of Sb_2Se_3/CdS were calculated from $N_{C\text{-}V}$-N_{DLCP} at zero V. The plots of $N_{C\text{-}V}$ and N_{DLCP} for S_{Mo1} and S_{Mo2} devices can be obtained from Equation 2 [33]:

$$\begin{cases} N_{\text{C-V}} = \dfrac{-2\varepsilon_{\text{r,n}} N_{\text{D}}}{\left(\dfrac{d(1/C^2)}{dV}\right) qA^2 \varepsilon_0 \varepsilon_{\text{r,n}} \varepsilon_{\text{r,p}} N_{\text{D}} + 2\varepsilon_{\text{r,p}}} \\ N_{\text{DLCP}} = -\dfrac{C_0{}^3}{2q\varepsilon_0 \varepsilon_{\text{r,p}} A^2 C_1} \\ x = \varepsilon_0 \varepsilon_{\text{r,p}} A / C_0 \end{cases} \tag{2}$$

where A is the area of solar cells, N_{D} is the carrier concentration of CdS, ε_0 is the permittivity of free space, and $\varepsilon_{\text{r,n}}$ and $\varepsilon_{\text{r,p}}$ are the relative permittivities of CdS and Sb_2Se_3 respectively. C_0 and C_1 were quadratic fitting parameters attained from the *C-V* data. The low discrepancy between the results of DLCP and the *C-V* of S_{Mo2} indicated minor interfacial defect concentration and less interface recombination than S_{Mo1} at the Sb_2Se_3/CdS interface. The concentrations of interfacial defect for S_{Mo1} and S_{Mo2} devices were 1.91×10^{16} and 5.50×10^{15} cm^{-3}, respectively. Moreover, the S_{Mo2} device possessed a larger depletion width (W_d) as compared with S_{Mo1} which was reasonable to occur since it varied positively with built-in voltage (V_{bi}), indicating the improved carrier transport in this high built-in electrical field, which improves the carrier transports. To further analyze the depletion region information and the mechanism behind the enhanced device performance, we performed *C-V* measurements. Fig. 5(b) shows the $1/C^2$-V curves. The V_{bi} extracted from the extended slope of the curves to the x-axis intercept for S_{Mo1} and S_{Mo2} devices were 533 and 582 mV, respectively. The MoO_2 IL improved the growth quality of Sb_2Se_3 absorber layer, which optimized the Sb_2Se_3/CdS heterojunction interface qualities. Thus, the MoO_2 IL increased the built-in voltage (V_{bi}) of Sb_2Se_3 solar cells, which led to the increased V_{OC}, J_{SC}, and FF of S_{Mo2}.

To further study the effect of MoO_2 IL on the bulk defect of Sb_2Se_3, we used admittance spectroscopy measurement to examine the energy levels of defects in the bandgap and defect density in the device. Fig. 5(c and d) shows the capacitance-frequency (*C-f*) results of S_{Mo1} and S_{Mo2} devices measured at different temperatures from 300 K to 180 K with an increment of 5

K. One defect level was witnessed in S_{Mo1} and S_{Mo2} devices. The inflection point corresponding to the admittance spectrum was determined by the Arrhenius plot. Its frequency value (ω_0) was obtained from the angular frequency point ω at the maximum of the $\omega dC/d\omega$ plot. The defect activation energies (E_a) were calculated from the slopes of Arrhenius plots that were linearly fitted based on Equation 3 [34–36].

$$\omega_0 = 2\pi\nu_0 T^2 \exp(\frac{-E_a}{kT}) \tag{3}$$

where ν_0 is the attempt-to-escape frequency, ω_0 is the inflection point frequency, k is the Boltzmann constant, and E_a is the defect activation energy representing the average defect energy level relative to the valence band maximum or conduction band minimum. According to the literature, the defect in the S_{Mo1} device with an E_a of 321 meV and the fault in the S_{Mo2} device with an E_a of 311 meV can be both referred to as Se vacancy (V_{Se}) (Fig. 5e) [37,38]. To further gain insights, we Gaussian fitted the distribution of each defect type using the Kimerling model based on the following equations [39].

$$E(\omega) = kT \ln(\frac{2\pi\nu_0 T^2}{\omega}) \tag{4}$$

$$N_t(E(\omega)) = -\frac{V_d}{q\omega}\frac{dC}{d\omega}\frac{\omega}{kT} \tag{5}$$

where built-in potential, angular frequency, and defect density are denoted as V_d, and ω, and $N_t(E(\omega))$, respectively. The defect densities of E_a values are given in Fig. 5(f). The calculated defect densities of S_{Mo1} and S_{Mo2} devices were 1.91×10^{16} and 6.64×10^{15} cm^{-3}, respectively. The MoO_2 IL reduced the device's defect density, resulting in less recombination at the interfacial and photo-absorber layers (Table 2).

Furthermore, carrier properties were obtained from temperature-dependent V_{OC} measurement. Fig. 6(a) illustrates the E_a of the main recombination in the solar cell. E_a of S_{Mo1} and S_{Mo2} devices were 0.95 and 1.16 eV, respectively. In comparison with that of S_{Mo1} device, the E_a of

S_{Mo2} device was relatively close to the band gap of Sb_2Se_3 (1.28 eV), which indicates weaker interfacial recombination in the S_{Mo2} device. For further study of the interface charge properties of devices, EIS measurements were used to characterize the Sb_2Se_3/CdS interface. Fig. 6(b) shows the Nyquist plots and the equivalent circuit model are illustrated. Recombination resistances (R) in S_{Mo1} and S_{Mo2} devices were calculated to be 17251 and 29717 Ω, respectively, and they were attained from the diameter of the arc. The higher R in S_{Mo2} confined the charge recombination at the Sb_2Se_3/CdS interface, which resulted in improved V_{OC}, J_{SC}, and FF. To further authenticate the boosted performance of S_{Mo2}, we systematically investigated the quality of the PN junction of S_{Mo1} and S_{Mo2} devices. Fig. 6(c) illustrates the dark J-V curves of S_{Mo1} and S_{Mo2} devices. Shunt conductance (G), diode ideality factor (A), series resistance (R), and reverse-saturation current density (J_0) were obtained from Equation (6) [40].

$$J = J_0 \exp\left[\frac{q}{AkT}(V - RJ)\right] + GV - J_{\mathrm{L}} \qquad (6)$$

Fig. 6(d) shows the dJ/dV versus V plot. The G values of S_{Mo1} and S_{Mo2} devices were 11.05 and 6.23 mS/cm^2, respectively. Both parameters (R and A) of the devices were obtained from dV/dJ against $(J+J_{SC})^{-1}$ (Fig. 6e). The R of S_{Mo1} and S_{Mo2} devices were 5.05 and 2.89 Ω·cm^2, respectively. The resulting value of R in S_{Mo2} device was smaller than that of S_{Mo1} device. In addition, the A of S_{Mo1} and S_{Mo2} devices were 2.34 and 1.79, respectively, implying the less interface recombination in S_{Mo2} device. By plotting $\ln(J+J_{SC}-GV)$ versus $V-RJ$ (Fig. 6f), the J_0 values of 1.1×10^{-3} and 8.94×10^{-4} mA/cm^2 were observed for S_{Mo1} and S_{Mo2} devices, respectively. Compared with the S_{Mo1} device, the S_{Mo2} device with MoO_2 IL had lower G, R, and A, which confirmed the improved Sb_2Se_3/CdS heterojunction quality.

4. Conclusions

In summary, we systematically improved the PV properties of Sb_2Se_3 solar cells by introducing MoO_2 IL to optimize Sb_2Se_3 crystal growth and back contact properties. MoO_2 IL successfully reduced the thickness of the $MoSe_2$ interface layer, and less void can be observed at the

Mo/Sb_2Se_3 interface. The back contact barrier of Mo/Sb_2Se_3 was lowered by the MoO_2 IL, which significantly increased the FF of the solar cell. The growth of (211)-oriented Sb_2Se_3 with large grains was induced by the MoO_2 IL. In addition, the introduction of MoO_2 IL not only improved the minority carrier diffusion length but also reduced the bulk defects of Sb_2Se_3 and interface defects at Sb_2Se_3/CdS, which inhibited the recombination of devices and improved the carrier transport. Thus, compared with that of S_{Mo1} solar cells without MoO_2 IL, the V_{OC} of the S_{Mo2} with MoO_2 layer increased from 0.481 V to 0.487 V and J_{SC} from 23.81 mA/cm^2 to 29.29 mA/cm^2 and attained a champion PCE of 8.14%. Our work provides an effective method to regulate Sb_2Se_3 crystal growth and back interface properties by introducing MoO_2 IL for highly efficient Sb_2Se_3 devices.

Acknowledgements

This work was supported by the National Natural Science Foundation of China (62074102), the Guangdong Basic and Applied Basic Research Foundation (2022A1515010979), the Key Project of Department of Education of Guangdong Province (2018KZDXM059), the Science and Technology plan project of Shenzhen (20220808165025003). The authors wish to acknowledge the assistance on HAADF-STEM observation received from the Electron Microscope Center of the Shenzhen University.

References

[1] M.A. Green, E.D. Dunlop, G. Siefer, M. Yoshita, N. Kopidakis, K. Bothe, X.J. Hao, Prog. Photovolt. 31 (2023) 3-16.

[2] Z. Li, X. Liang, G. Li, H. Liu, H. Zhang, J. Guo, J. Chen, K. Shen, X. San, W. Yu, R.E.I. Schropp, Y. Mai, Nat. Commun. 10 (2019) 1-9.

[3] X. Wen, C. Chen, S. Lu, K. Li, R. Kondrotas, Y. Zhao, W. Chen, L. Gao, C. Wang, J.

Zhang, G. Niu, J. Tang, Nat. Commun. 9 (2018) 2179.

[4] L. Wang, D.B. Li, K. Li, C. Chen, H.X. Deng, L. Gao, Y. Zhao, F. Jiang, L. Li, F. Huang, Y. He, H. Song, G. Niu, J. Tang, Nat. Energy 2 (2017) 17046.

[5] K.H. Li, Y. Lu, X.K. Yang, L.C. Fu, J.G. He, X.T. Lin, J.J. Zheng, S.C. Lu, C. Chen, J. Tang, InfoMat 3 (2021) 1145.

[6] J. Tao, X. Hu, Y. Guo, J. Hong, K. Li, J. Jiang, S. Chen, C. Jing, F. Yue, P. Yang, C. Zhang, Z. Wu, J. Tang, J. Chu, Nano Energy 60 (2019) 802–809.

[7] R. Tang, Z.H. Zheng, Z.H. Su, X.J. Li, Y.D. Wei, X.H. Zhang, Y.Q. Fu, J.T. Luo, P. Fan, G.X. Liang, Nano Energy 64 (2019) 103929.

[8] Y.D. Luo, R. Tang, S. Chen, J.G. Hu, Y.K. Liu, Y.F. Li, X.S. Liu, Z.H. Zheng, Z.H. Su, X.F. Ma, P. Fan, X.H. Zhang, H.L. Ma, Z.G. Chen, G.X. Liang, Chemical Engineering Journal 393 (2020) 124599.

[9] G.X. Liang, Y.D. Luo, S. Chen, R. Tang, Z.H, Zheng, X.J. Li, X.J. Liu, Y.X. Liu, Y.K. Li, X.Y. Chen, Z.H. Su, X.H. Zhang, H.L. Ma, P. Fan, Nano Energy 73 (2020) 104806.

[10] K.J. Tiwari, M. Neuschitzer, M. Espíndola-Rodriguez, Y. Sánchez, Z. Jehl, P. Vidal-Fuentes, E. Saucedo, P. Malar, Sol. Energy Mater. Sol. Cells 215 (2020) 110603.

[11] W.H. Wang, Z.X. Cao, X. Zuo, L. Wu, J.S. Luo, Y. Zhang, J. Energy Chem. 70 (2022) 191-200.

[12] L. Guo, B. Zhang, S. Ranjit, J. Wall, S. Saurav, A.J. Hauser, G. Xing, L. Li, X. Qian, F. Yan, Sol. RRL 3 (2019) 900225.

[13] L. Guo, B. Zhang, Y. Qin, D. Li, L. Li, X. Qian, F. Yan, Sol. RRL 2 (2018) 1800128.

[14] Z. T. Duan, X.Y. Liang, Y. Feng, H.Y. Ma, B.L. Liang, Y. Wang, S.P. Luo, S.F. Wang, R.E.I. Schropp, Y.H. Mai, Z.Q. Li, Adv. Mater. 34 (2022) 2202969.

[15] Y.Q. Zhao, S.Y. Wang, C. Li, B. Che, X.L. Chen, H.Y. Chen, R.F. Tang, X.M. Wang, G.L. Chen, T. Wang, J.B. Gong, T. Chen, X.D. Xiao, J.M. Li, Energy Environ. Sci. 15 (2022) 5118-5128.

[16] C Liu, S. H Wu, Y. Y Gao, Y Feng, X. L Wang, Y. F Xie, J. Z Zheng, H. B Zhu, Z. Q Li, R. E. I. Schropp, K Shen, Y. H Mai, Adv. Funct. Mater. 32 (2022) 2209601.

[17] X.S. Liu, J. Chen, M. Luo, M.Y. Leng, Z. Xia, Y. Zhou, S.K. Qin, D.J. Xue, L. Lv, H. Huang, D.M. Niu, J. Tang, ACS Appl. Mater. Interfaces 6 (2014) 10687-10695.

[18] Y. Zhou, L. Wang, S.Y. Chen, S.K. Qin, X.S. Liu, J. Chen, D.J. Xue, M. Luo, Y.Z. Cao, Y.B. Cheng, E.H. Sargent, J. Tang, Nat. Photon. 9 (2015) 409–415.

[19] R.F. Tang, X.M. Wang, W.T. Lian, J.L. Huang, Q. Wei, M.L. Huang, Y.W. Yin, C.H. Jiang, S.F. Yang, G.C. Xing, S.Y. Chen, C.F. Zhu, X.J. Hao, M.A. Green, Nat. Energy 5(2020) 587.

[20] Q. Yan, Q.Z. Sun, H. Deng, W.H. Xie, C.X. Zhang, J.H. Wu, Q. Zheng, S.Y. Cheng, J. Energy Chem. 75 (2022) 8-15.

[21] J.M. Burst, J.N. Duenow, D.S. Albin, E. Colegrove, M.O. Reese, J.A. Aguiar, C.S. Jiang, M.K. Patel, M.M. Al-Jassim, D. Kuciauskas, S. Swain, T. Ablekim, K.G. Lynn, W.K. Metzger, Nat. Energy 1 (2016) 16015.

[22] J.H. Tang, X.S. Yin, G.J. Qi, H. Gong, Phys. Status Solidi Rapid Res. Lett. 8 (2014) 735-762.

[23] R. Tang, S. Chen, Z.H. Zheng, Z.H. Su, J.T. Luo, P. Fan, X.H. Zhang, J. Tang, G.X. Liang, Adv. Mater. 14 (2022) 2109078.

[24] J.H. Lin, A. Mahmood, G.J. Chen, N. Ahmad, M.D. Chen, P. Fan, S. Chen, R. Tang, G.X. Liang, Mater. Today Phys. 27 (2022) 100772.

[25] Z.Q. Li, X. Chen, H.B. Zhu, J.W. Chen, Y.T. Guo, C. Zhang, W. Zhang, X.N. Zhang, X.N. Niu, Y.H. Mai, Sol. Energy Mater. Sol. Cells 161 (2017) 190-196.

[26] L. Guo, B. Zhang, S. Li, Q. Zhang, M. Buettner, L. Li, X. Qian, F. Yan, Apl. Mater. 7 (2019) 041105.

[27] D. Cozza, C.M. Ruiz, D. Duché, J.J. Simon, L. Escoubas, IEEE J Photovolt 6 (2016) 1292-1297.

[28] Y.H. Zhao, Z.X. Yu, J.G. Hu, Z.H. Zheng, H.L. Ma, K.W. Sun, X.J. Hao, G.X. Liang, P. Fan, X.H. Zhang, Z.H. Su, J. Energy Chem. 75 (2022) 321-329.

[29] A. Amin, D. Li, X.M. Duan, S.N. Vijayaraghavan, H.G. Menon, J. Wall, M. Weaver, M.M.C. Cheng, Y.F. Zheng, L. Li, F. Yan, Adv. Mater. Interfaces. (2022) 2200547.

[30] S.N. Park, S.Y. Kim, S.J. Lee, S.J. Sung, K.J. Yang, J.K. Kang, D.H. Kim, J. Mater. Chem. 7 (2019) 25900-25907.

[31] O. Gunawan, T.K. Todorov, D.B. Mitzi, Appl. Phys. Lett. 97 (2010) 233506.

[32] G.S. Park, V.B. Chu, B.W. Kim, D.W. Kim, H.S. Oh, Y.J. Hwang, B.K. Min, ACS Appl. Mater. Interfaces 10 (2018) 9894-9899.

[33] M. Luo, M.Y. Leng, X.S. Liu, J. Chen, C. Chen, S.K. Qin, J. Tang, Appl. Phys. Lett. 104 (2014) 173904.

[34] X. Hu, J. Tao, G. Weng, J. Jiang, S. Chen, Z. Zhu, J. Chu, Sol. Energy Mater. Sol. Cells 186 (2018) 324-329.

[35] T. Eisenbarth, T. Unold, R. Caballero, C.A. Kaufmann, H.W. Schock, J. Appl. Phys. 107 (2010) 034509.

[36] T. Walter, R. Herberholz, C. Müller, H.W. Schock, J. Appl. Phys. 80 (1996) 4411-4420.

[37] X.S. Liu, X. Xiao, Y. Yang, D.J. Xue, D.B. Li, C. Chen, S.C. Lu, L. Gao, Y.S. He, M.C. Bread, G. Wang, S.Y. Chen, J. Tang, Prog. Photovoltaics Res. Appl. 25 (2017) 861-870.

[38] M.L. Huang, P. Xu, D. Han, J. Tang, S.Y. Chen, ACS Appl. Mater. Interfaces 11 (2019) 15564-15572.

[39] J. Li, S. Kim, D. Nam, X. Liu, J. Kim, H. Cheong, W. Liu, H. Li, Y. Sun, Y. Zhang, Sol. Energy Mater. Sol. Cells 159 (2017) 447-455.

[40] M. Ishaq, H. Deng, S. Yuan, H. Zhang, J. Khan, U. Farooq, H. Song, J. Tang, Sol. RRL 2 (2018) 1800144.

Table 1. The photovoltaic parameters of S_{Mo1}, S_{Mo2} and S_{Mo3} devices.

Devices	V_{OC} (V)	J_{SC} (mA/cm^2)	FF (%)	PCE (%)
S_{Mo1}	0.481	23.81	50.28	5.75
S_{Mo2}	0.487	29.29	57.10	8.14
S_{Mo3}	0.424	21.52	45.76	4.18

Table 2. Summary of the results derived from CV, DLCP and AS measurement.

Devices	N_{CV} (cm^{-3})	N_{DLCP} (cm^{-3})	Interface defect density (cm^{-3})	V_{bi} (mV)	W_d (nm)
S_{Mo1}	8.11×10^{16}	6.20×10^{16}	1.91×10^{16}	533	0.281
S_{Mo2}	6.71×10^{16}	6.16×10^{16}	5.50×10^{15}	582	0.290

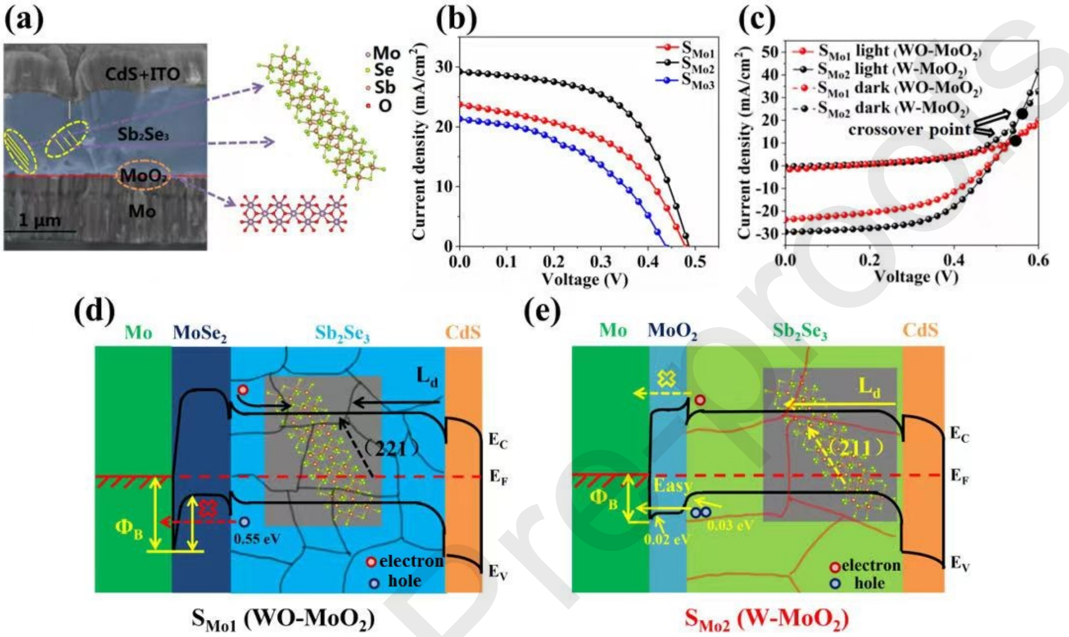

Fig. 1. (a) Cross-sectional SEM image of S_{Mo2} device. (b) *J-V* curves of S_{Mo1}, S_{Mo2} and S_{Mo3} devices. (c) *J-V* curves of S_{Mo1} and S_{Mo2} devices under light and dark states. (d) The band diagrams of S_{Mo1}. (e) The band diagrams of S_{Mo2} devices.

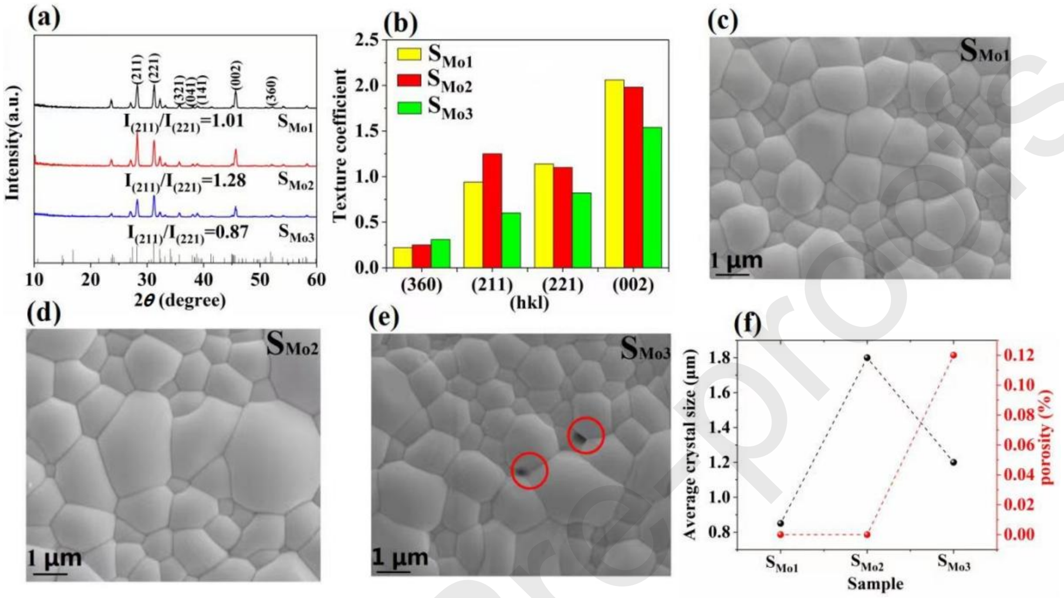

Fig. 2. (a) XRD patterns of Sb_2Se_3 thin films. (b) Texture coefficients of the diffraction peaks of Sb_2Se_3 thin films. (c-e) Surface morphologies of Sb_2Se_3 thin films. (f) The average crystal sizes and porosity of Sb_2Se_3 thin films.

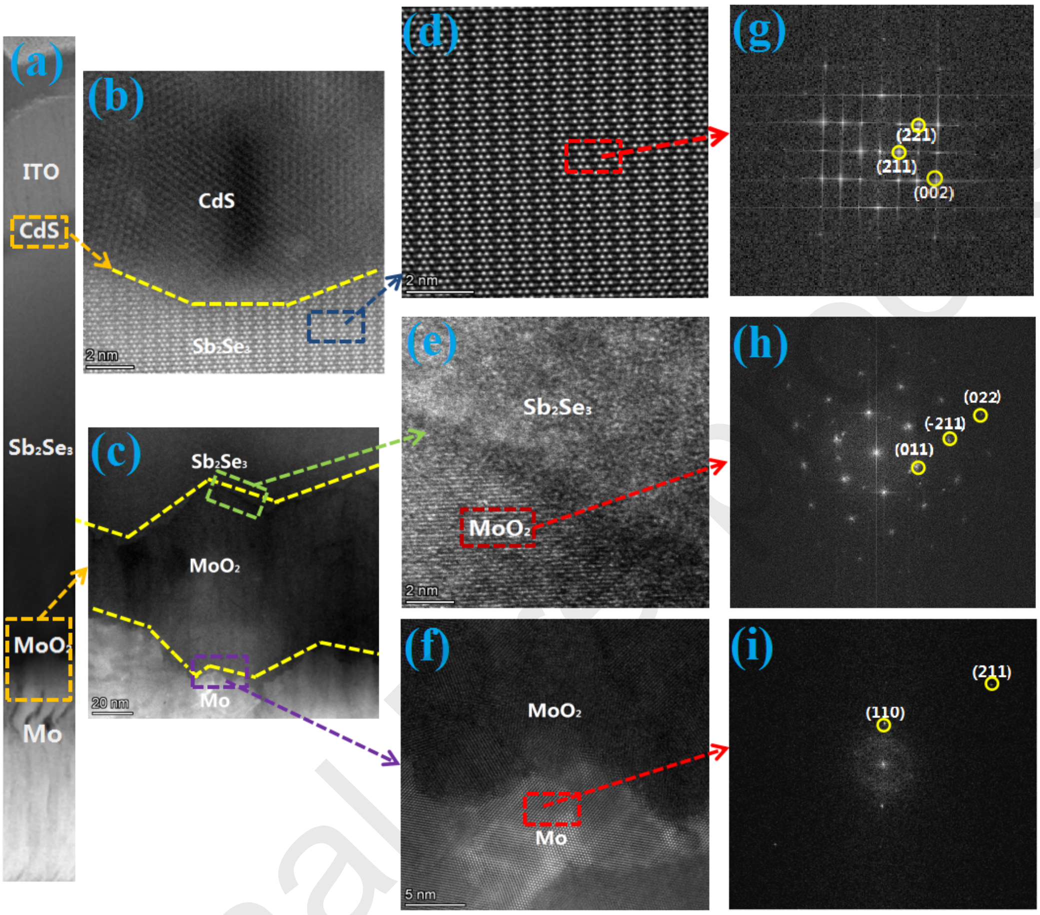

Fig. 3. (a) Cross-sectional TEM image of S_{Mo2} device. (b) Sb_2Se_3/CdS interface TEM image. (c) Mo/MoO_2/Sb_2Se_3 back contact TEM images. (d-f) High-resolution TEM images of Sb_2Se_3 absorber layer, MoO_2/Sb_2Se_3 interface, and Mo/MoO_2 interface. (g-i) The SAED patterns of Sb_2Se_3 absorber layer, MoO_2/Sb_2Se_3 interface, and Mo/MoO_2 interface.

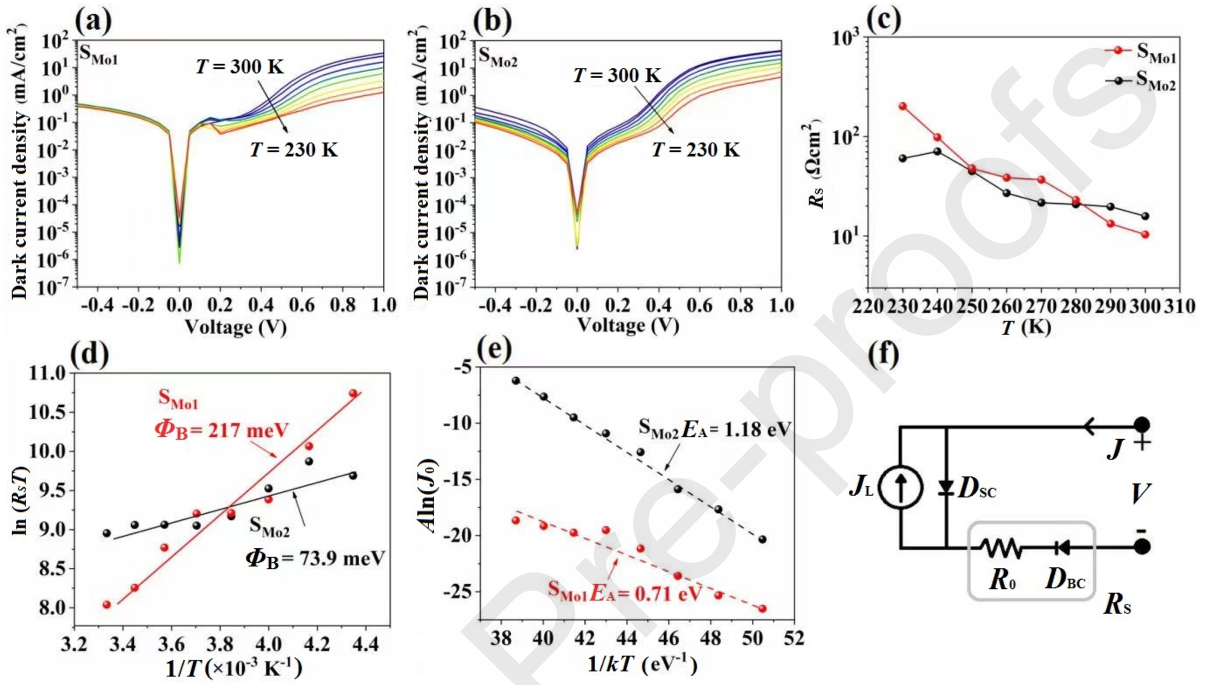

Fig. 4. (a and b) Temperature-dependent dark current density vs voltage characteristics for a temperature range of approximately 300 to 230 K for devices. (c) Temperature-dependent R_s of the devices. (d) Blocking contact barrier height of the devices. (e) Aln(J_0) vs 1/kT plot of S_{Mo1} and S_{Mo2} devices. (f) Circuit model illustrating the solar cell diode (D_{SC}), photogenerated current source (J_L), and the lumped-series resistance (R_S) consisting of background or residual series resistance (R_0) and a blocking back contact diode (D_{BC}).

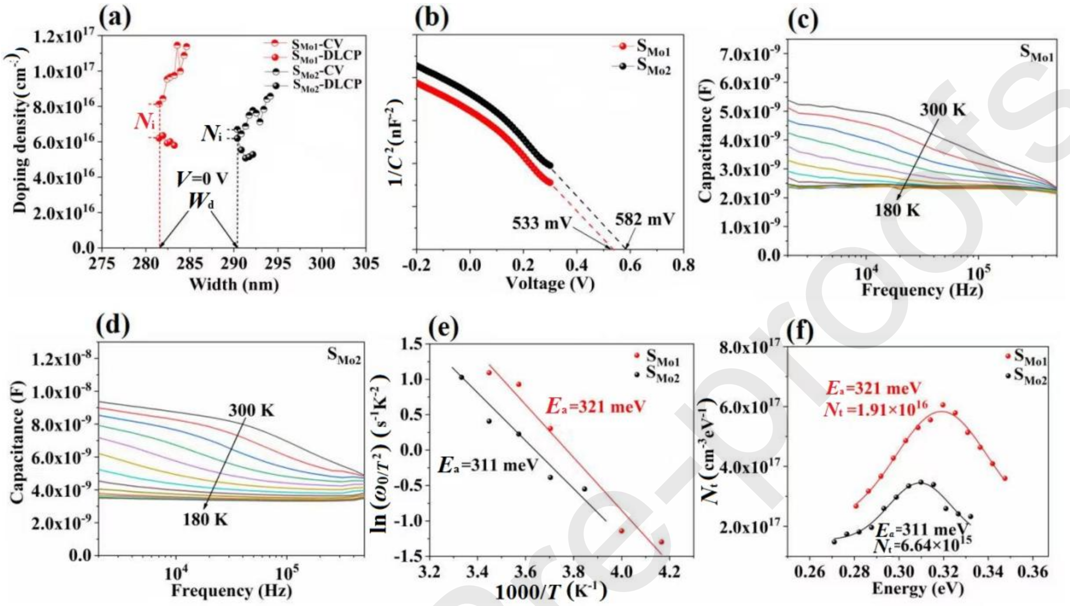

Fig. 5. (a) *C-V* and *DLCP* profiles of the S_{Mo1} and S_{Mo2} devices. (b) $1/C^2$-V plots of the S_{Mo1} and S_{Mo2} devices. (c and d) Temperature-dependent admittance results for the S_{Mo1} and S_{Mo2} devices. (e) Arrhenius plots of ω_0/T^2 versus 1000/T for two devices; the defect activation energies (E_a) were calculated for the defect and are shown inside the figure. (f) Defect densities and defect activation energies (E_a) of S_{Mo1} and S_{Mo2} devices derived from the admittance spectra.

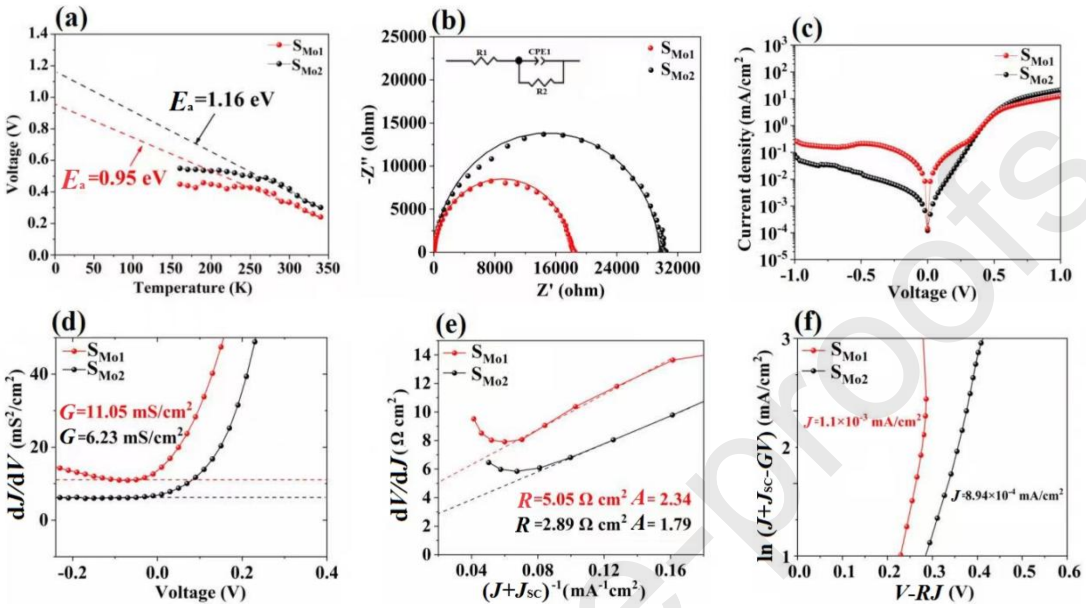

Fig. 6. (a) Temperature-dependent V_{OC} measurements. (b) Nyquist plots of S_{Mo1} and S_{Mo2} devices. (c) Dark *J-V* curves of S_{Mo1} and S_{Mo2} devices. (d) Shunt conductance *G* of S_{Mo1} and S_{Mo2} devices. (e) Series resistance *R* and ideality factor *A* of S_{Mo1} and S_{Mo2} devices. (f) Reverse saturation current density J_0 of S_{Mo1} and S_{Mo2} devices.

Graphical abstract

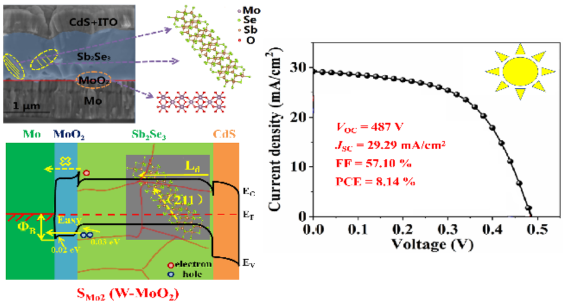

The MoO_2 intermediate layer enhanced the growth of (211) oriented Sb_2Se_3 absorber and the transport of photo-generated hole at the back contact. The power conversion efficient (PCE) of Sb_2Se_3 solar cell was improved to 8.14 %.

Supporting Information

Back contact interfacial modification mechanism in highy-efficient antimony selenide thin-film solar cells

Jun-Hui Lin[1], *Guo-Jie Chen*[1], *Nafees Ahmad*[1], *Muhammad Ishaq*[2], *Shuo Chen*[1], *Zheng-Hua Su*[1], *Ping Fan*[1], *Xiang-Hua Zhang*[3], *Yi Zhang*[4], *Guang-Xing Liang*[1]*

[1.] *Shenzhen Key Laboratory of Advanced Thin Films and Applications, Key Laboratory of Optoelectronic Devices and Systems of Ministry of Education and Guangdong Province, College of Physics and Optoelectronic Engineering, Shenzhen University, Shenzhen 518060, Guangdong, China.*

[2.] *Institute of Fundamental and Frontier Science, University of Electronic Science and Technology of China. Chengdu 610054, Sichuan. China*

[3.] *Univ Rennes, CNRS, ISCR (Institut des Sciences Chimiques de Rennes) UMR 6226, Rennes, F-35000, France*

[4.] *Institute of Photoelectronic Thin Film Devices and Technology and Tianjin Key Laboratory of Thin Film Devices and Technology, Nankai University, Tianjin 300350, China.*

*Corresponding author. E-mail address: lgx@szu.edu.cn (Prof. Liang).

Table S1. EDS results for Sb_2Se_3 thin films with different Mo substrates.

Sample	Sb (at. %)	Se (at. %)	Sb/Se ratio
S_{Mo1}	35.54	64.46	0.55
S_{Mo2}	38.09	61.91	0.62
S_{Mo3}	40.68	59.32	0.69

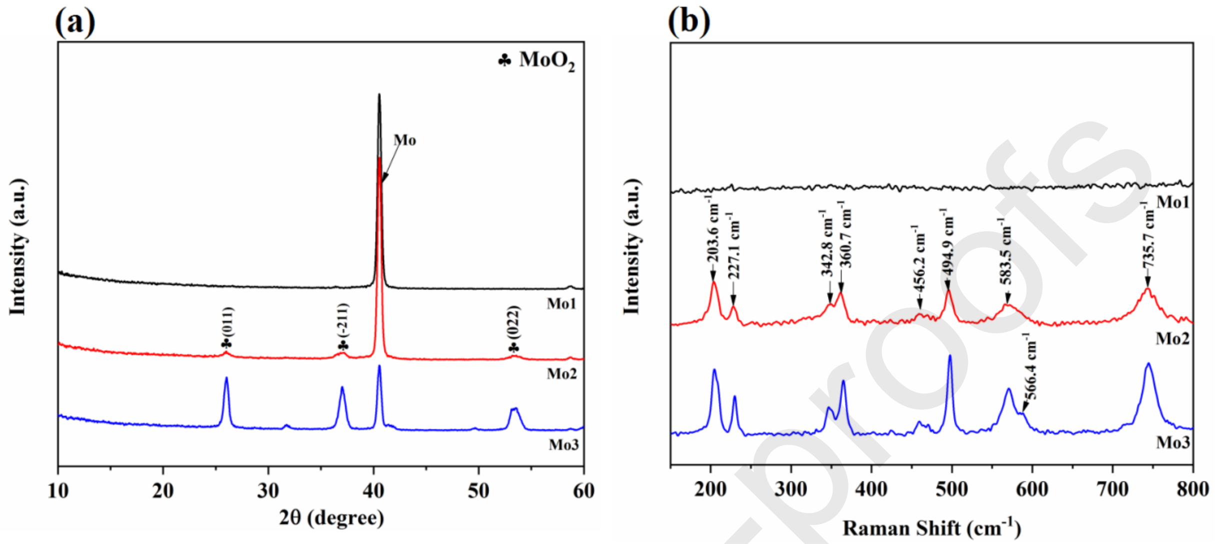

Fig. S1. (a) XRD patterns of Mo1, Mo2, and Mo3 substrates, and (b) Raman spectra of the surface of Mo1, Mo2, and Mo3 substrates.

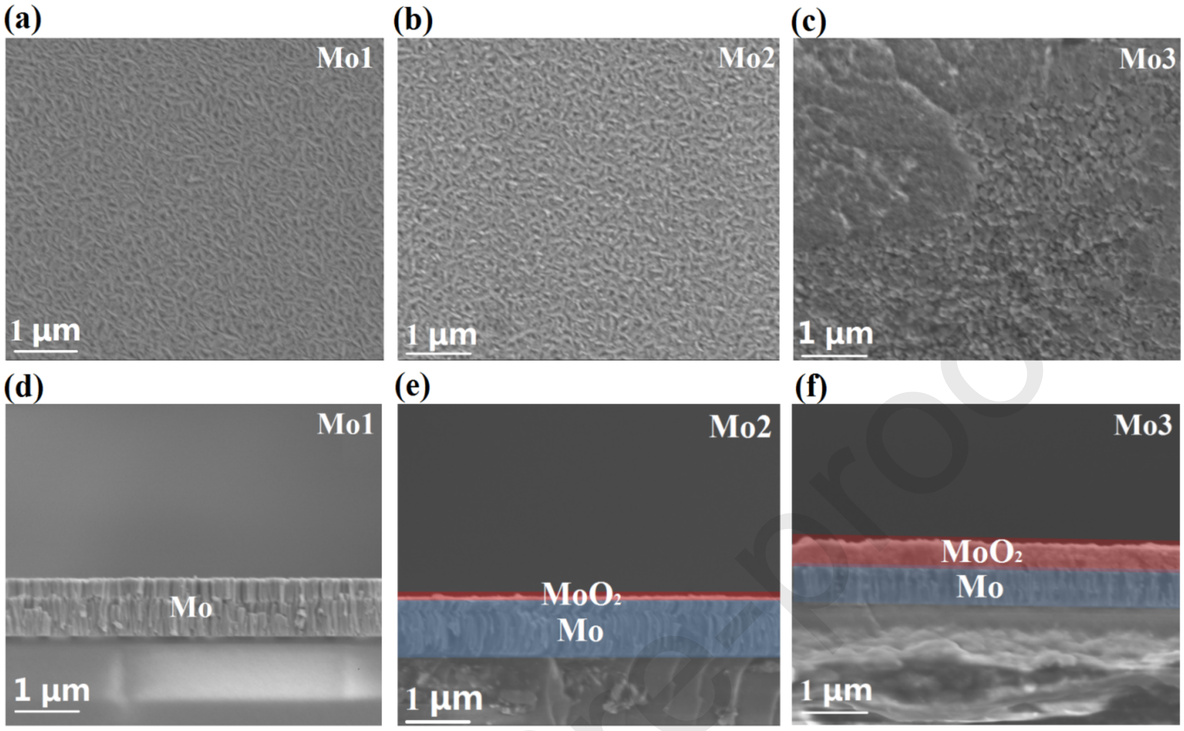

Fig. S2. (a-b) Surface SEM images of Mo substrates, and (d-f) cross-sectional SEM images of Mo substrates

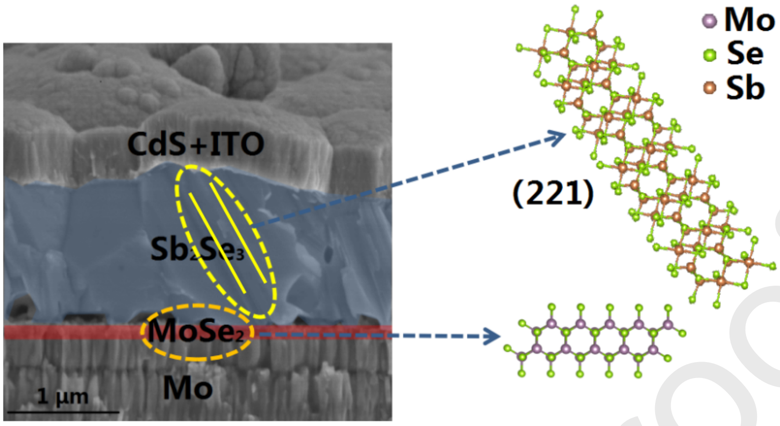

WO- MoO_2 intermediate layer

Fig. S3. Cross-sectional SEM image of S_{Mo1} device (WO-MoO_2 intermediate layer)

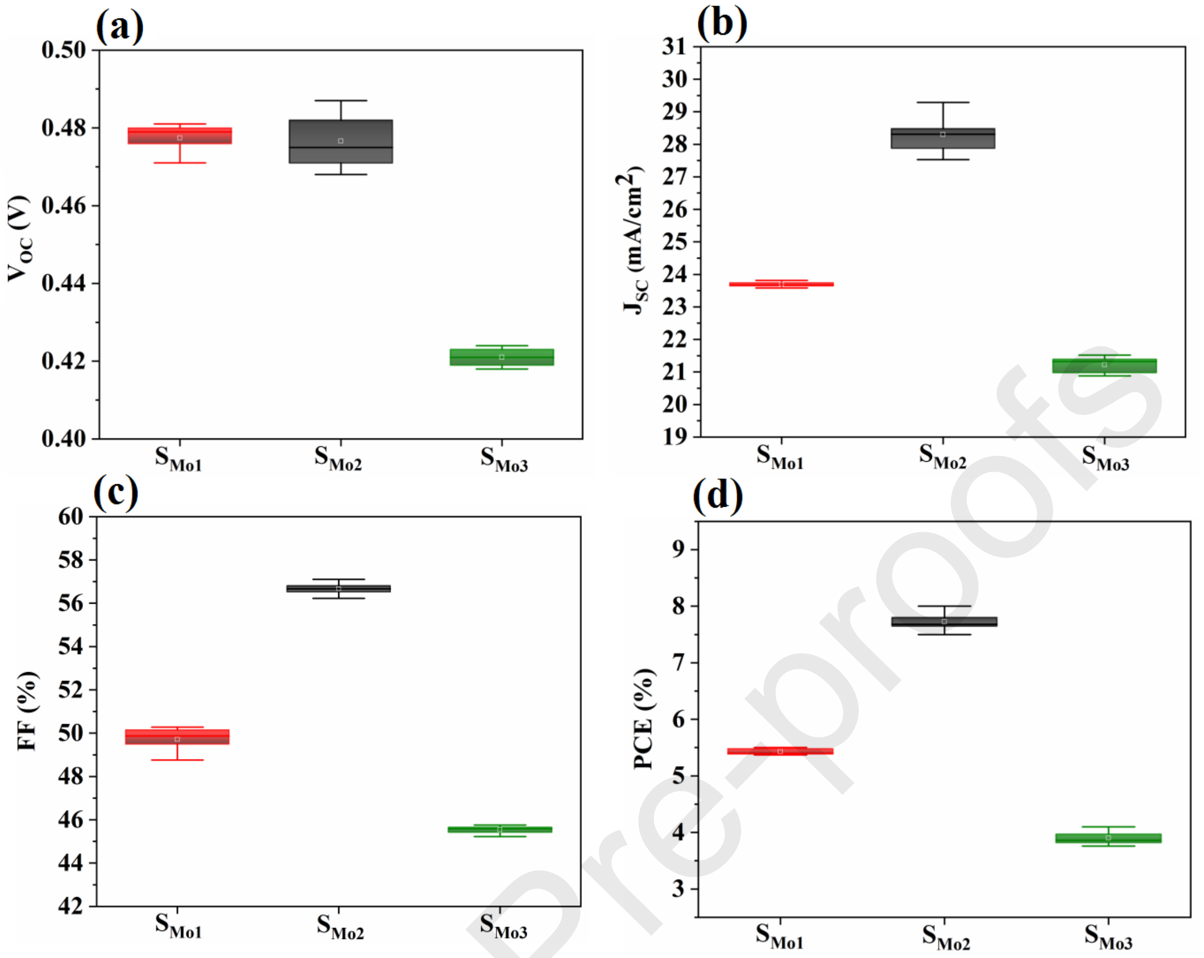

Fig. S4. Statistical distribution of the devices performance parameters including (a) open-circuit voltage (V_{OC}), (b) short-circuit current density (J_{SC}), (c) fill factor (FF), and (d) power conversion efficiency (PCE).

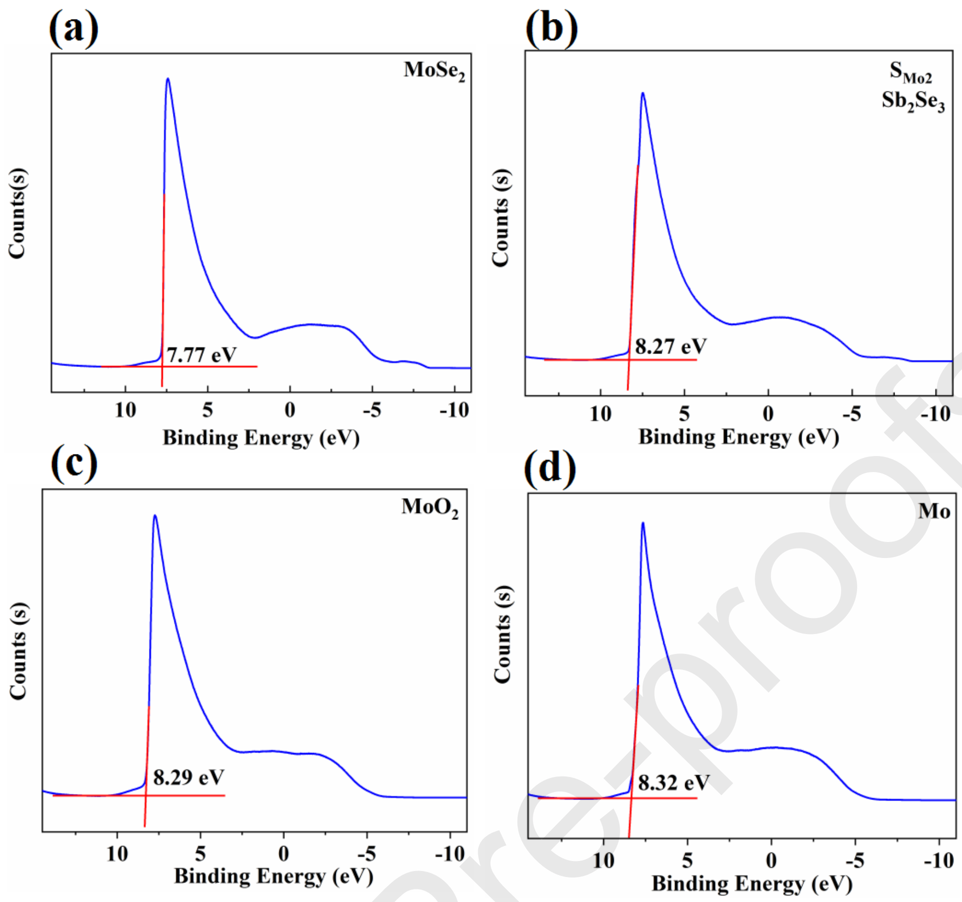

Fig. S5. UPS spectra for (a) the surface of $MoSe_2$ interface layer, (b) the back of Sb_2Se_3 layer in S_{Mo2} device, (c) the surface of MoO_2 intermediate layer, and (d) the surface of Mo.

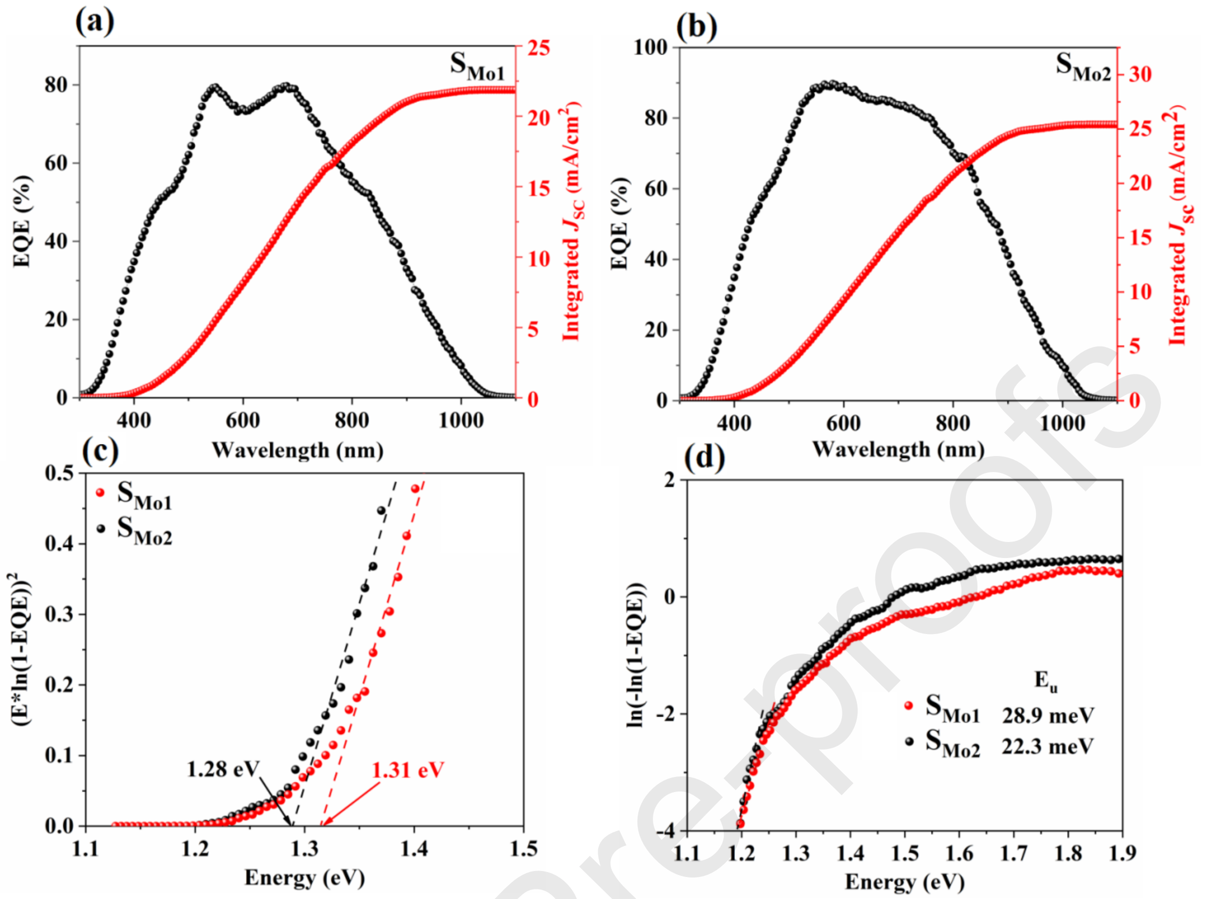

Fig. S6. (a) EQE and integarated J_{SC} of S_{Mo1} device, (b) EQE and integarated J_{SC} of S_{Mo2} device, (c) bandgap obtained from the EQE of solar cells, and (d) Urbach energy (E_u) obtained from the EQE of solar cells.

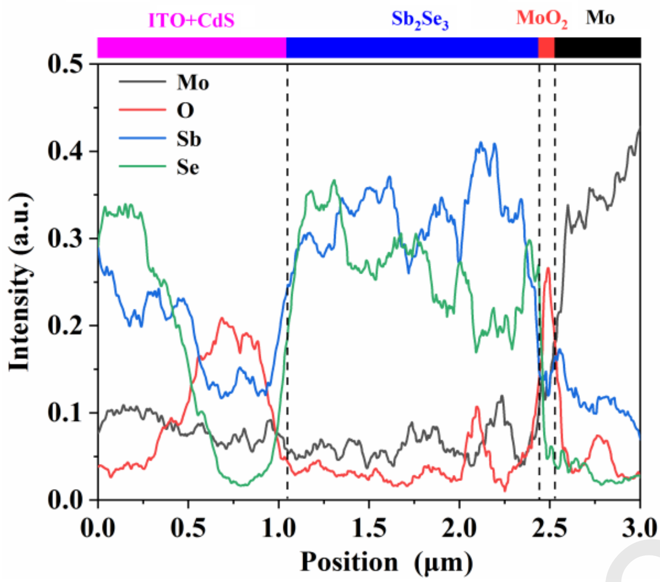

Fig. S7. EDS element depth profiles of Mo, O, Sb and Se elements in S_{Mo2} device.

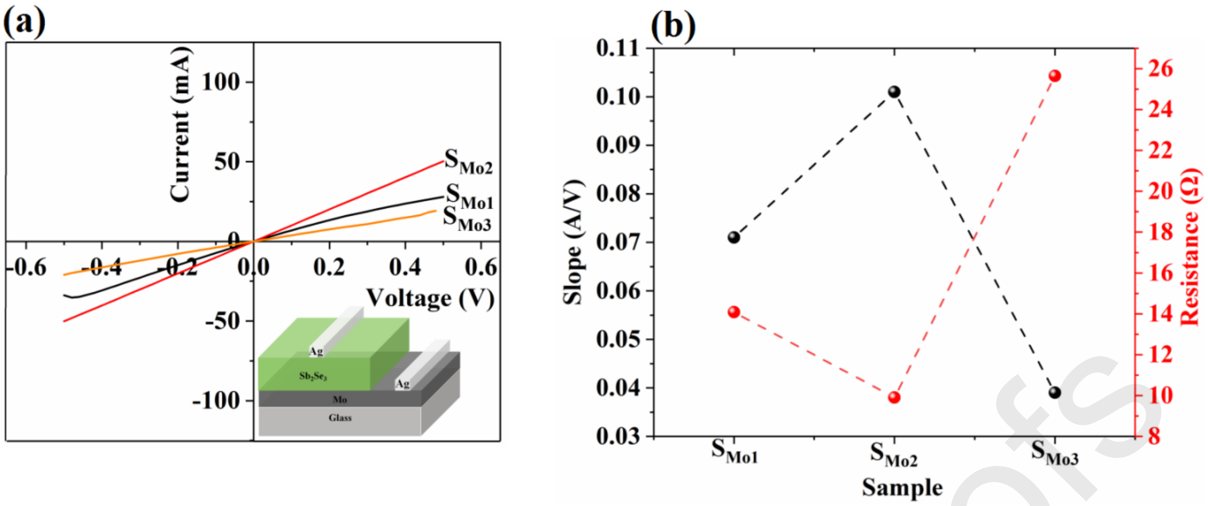

Figure S8. (a) *I-V* curves of Mo/Sb_2Se_3 back contact (the schematic diagram of structure used to test *I-V* curves was inserted). (b) The slopes and resistance curves of S_{Mo1}, S_{Mo2}, and S_{Mo3} samples.

Highlights

☐ MoO2 layer induces the growth of (211) oriented Sb2Se3 with large grains.
☐ Low back contact barrier can be achieved by introducing the MoO2 layer.
☐ The carrier recombination, bulk and interfacial defects can be passivated.
☐ Highly efficiency of 8.14% obtained by back contact optimization.

Declaration of interests

☒ The authors declare that they have no known competing financial interests or personal relationships that could have appeared to influence the work reported in this paper.

☐ The authors declare the following financial interests/personal relationships which may be considered as potential competing interests: